Fast Approach for Battery Impedance Identification Using Pseudo-Random Sequence Signals

Jussi Sihvo, *Student Member, IEEE*, Daniel-Ioan Stroe, *Member, IEEE*, Tuomas Messo, *Member, IEEE*, and Tomi Roinila, *Member, IEEE*

***Abstract*—Online measurements of the battery impedance provide valuable information on the battery state-of-charge and state-of-health, which can be utilized for improving the safety and the performance of the associated system. The electrochemical-impedance spectroscopy (EIS) is widely used for battery impedance measurements, but it is not the most applicable solution for online measurements due to its slowness and complexity. These drawbacks can be improved using broadband signals, such as pseudorandom sequences (PRS), which are fast and easily implementable. However, the nonlinear behavior of batteries have a significant effect on the impedance measurements and the selection of the PRS signal. Majority of the PRS signals are applicable for measurements of linear systems, but also signals for nonlinear system identification do exist. Moreover, the reduced accuracy and signal-to-noise ratio of the PRS signals compared to the EIS make the filtering of the results as well as the amplitude design important aspects. This paper demonstrates the use of two PRS signals, the pseudorandom binary sequence (PRBS), and a ternary sequence with better toleration to battery nonlinear effects, with comprehensive amplitude and filtering design for battery impedance measurements. It is shown that the ternary sequence provides accurate measurements and the effects of nonlinear dynamics of the battery impedance are reduced with respect to the PRBS measurements. The results are referenced and validated to practical EIS measurements in various operating conditions for lithium-iron-phosphate ($LiFePO_4$) cell.**

***Index Terms*—Batteries, energy storage, impedance measurement, real-time systems.**

I. Introduction

THE use of lithium-ion (Li-Ion) batteries in electric vehicles and stationary storage applications have become extremely popular in recent years. This is mainly due to their high energy and power density, high efficiency, long lifetime, and continuously reduced price [1], [2].

The Li-ion batteries are usually equipped with a battery-management system (BMS) that monitors the battery conditions to ensure its safe operation [3]. Typically, the BMS monitors the battery current, voltage, and temperature, which are further used to estimate the battery state. The battery state is expressed by different state parameters such as the state-of-charge (SOC) and the state-of-health (SOH). The SOC indicates the remaining charge that can be drawn from the battery [4]. The SOH indicates the remaining useful life of the battery for the application [5]. However, the accurate estimation of the SOC and the SOH is difficult due to their nonlinear dependence to the monitored quantities.

For the battery state-estimation and modeling purposes, the battery ac impedance has recently gained much research interest, since it has significant relation to the battery aging [6]–[8] and the SOC [9]–[12] as well as to the temperature [13]. In the impedance-based state estimation, the impedance is typically fitted to an equivalent circuit model and the state estimation is based on the variations in the model parameters [9]–[11], [14]. Therefore, the impedance online measurements have recently become important to utilize the impedance for the state estimation of Li-ion batteries. The impedance is conventionally characterized by the electrochemical-impedance spectroscopy (EIS), which utilizes a sinusoidal excitation [14]–[16]. The method provides accurate measurements but comes with high complexity and long measurement time, which makes it challenging to be utilized in online applications. For online use, methods such as simplified EIS [17]–[19], square-sweep [20], steps [21]–[24], multisines [24], [25], and pseudorandom sequences (PRS) are studied. Especially the PRS methods are attractive alternatives due to their low complexity, low measurement time, and relatively good accuracy. The PRS signals are studied in [20], [26], and [27], where the two-level pseudorandom binary sequence (PRBS) is applied for battery impedance measurements but are reported to suffer from reduced measurement accuracy under battery nonlinearities. However, the excitation performance for nonlinear systems can be improved with multilevel PRS signals [28]–[31]. From such PRS signals, a three-level ternary sequence have been studied in [32] for battery impedance measurement, where it showed to provide accurate results under battery nonlinearities.

Manuscript received January 14, 2019; revised March 27, 2019; accepted June 16, 2019. Date of publication July 1, 2019; date of current version December 13, 2019. This work was supported by Tiina and Antti Herlin Foundation, as well as, the Academy of Finland. Recommended for publication by Associate Editor D. Maksimovic. *(Corresponding author: Jussi Sihvo.)*

J. Sihvo and T. Messo are with the Faculty of Information Technology and Communication Sciences, Tampere University, Tampere 33100, Finland (e-mail: jussi.sihvo@tuni.fi; tuomas.messo@tuni.fi).

D.-I. Stroe is with the Department of Energy Technology, Aalborg University, Aalborg 9100, Denmark (e-mail: dis@et.aau.dk).

T. Roinila is with the Faculty of Engineering and Natural Sciences, Tampere University, Tampere 33100, Finland (e-mail: tomi.roinila@tuni.fi).

Color versions of one or more of the figures in this paper are available online at http://ieeexplore.ieee.org.

Digital Object Identifier 10.1109/TPEL.2019.2924286

The low measurement time of the PRS signals compared to the EIS method comes at the expense of reduced accuracy and signal-to-noise ratio (SNR) since the signal power is divided into several frequency harmonics instead of one fundamental harmonic [28]. The SNR of the PRS is given by the length and the amplitude of the signal that together determine the power content of the signal. Increased amplitude of the PRS increases also the SNR, but this can introduce more nonlinear effects in the battery and can be even limited by the application [33]. The SNR can also be increased by shortening the sequence length, but this will reduce the bandwidth of the measurements by making the frequency resolution more sparse. In addition, filtering can be applied to smooth the measurements and increase the SNR. The moving-average filter (MAF) is a good alternative due to its simplicity but careful window design is required to keep the data uncorrupted [34]. Thus, the PRS frequency content, amplitude design, and the effect of filtering needs to be carefully studied to obtain reliable results.

This paper provides a comprehensive study of fast impedance measurement techniques for Li-ion batteries using two different PRS excitation signals, the PRBS and the ternary sequence, with optimized amplitude and MAF design. The performance of both PRS methods are studied in various operating conditions for lithium–iron–phosphate ($LiFePO_4$) battery cell. The results are validated by means of EIS reference data with error analysis based on the root-mean-square error (RMSE). Moreover, a linear Kronig–Kramers compliance test is applied to analyze the quality of the measured impedances [35].

The rest of the paper is organized as follows. The impedance characteristics and relation to battery state parameters are introduced in Section II. The generation algorithms and properties of the PRS signals are studied in Section III. The experiments, including the amplitude and filtering design, are presented in Section IV. The performance validation is carried out in Section V, and the conclusions are drawn in Section VI.

II. Internal Impedance Relation to Battery State

The impedance of a battery is a parasitic quantity that resists the current flow through the battery. The impedance introduces a voltage drop to the battery open-circuit voltage whenever any current is applied to the battery. The impedance is a frequency-dependent quantity and can be represented in frequency domain as

$$Z_{\text{bat}}(j\omega) = \frac{V_{\text{bat}}(j\omega)}{I_{\text{bat}}(j\omega)} \tag{1}$$

where $V_{\text{bat}}(j\omega)$ is the battery terminal voltage, $I_{\text{bat}}(j\omega)$ is the battery current, and ω is the angular frequency.

The impedance is typically represented in the Nyquist-plane (commonly known as complex-plane) shown in Fig. 1 from which usually three or four main regions can be detected caused by different electrochemical phenomenons. The diffusion part at low frequencies represents the effect of the solid-state diffusion of Li-ion between the electrodes, which results in a constant slope. The charge-transfer region represents the charge-transfer phenomenon at the electrode surfaces. It is usually formed as

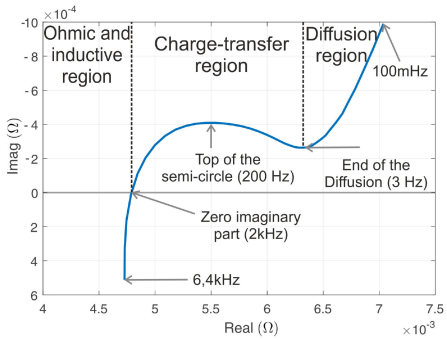

Fig. 1. Impedance Nyquist plot from $LiFePO_4$ cell.

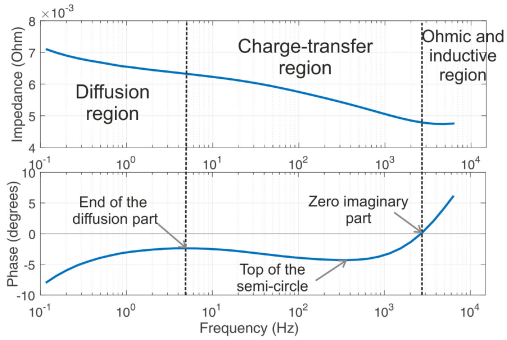

Fig. 2. Impedance Bode plot from $LiFePO_4$ cell.

one or more semicircles mostly depending on the battery chemistry and temperature at the medium frequencies. The ohmic region represents the region where the impedance intersects the real-axis. At the very high frequencies (>10 kHz), an inductive region can also be detected, which is caused by the inductance of the wires and current collectors of the battery. Moreover, the shape of the impedance in the described regions also varies as a function of the temperature, the SOC and the SOH [7], [25]. The corrosion on the electrolyte and on electrodes, lithium plating, and especially the formation of the solid-electrolyte-interface layer increase the impedance as the battery ages. The increase in the temperature accelerates the chemical reactions in the battery, thus, reducing the magnitude of the impedance. However, high temperatures also accelerates the aging of the battery, which will eventually increase the impedance magnitude in the long run [7]. The impedance also changes as the function of the SOC, especially at very low and high SOC values [8], [13].

Alternatively, the impedance can be also represented as a Bode diagram with separate magnitude and phase responses as shown in Fig. 2. The benefit of the Bode diagram is the provided frequency information, which cannot be seen in the Nyquist-plane. The same information about the impedance behavior is still provided in the Bode diagram where the bounds for each region are given by the phase behavior. The Bode diagram can be an effective tool for optimizing the bandwidth and the resolution of the measurements to include only the parts of the impedance that are in the range of interest.

III. Internal Impedance Measurement Techniques

A typical device under test measurement setup is illustrated in Fig. 3, where $x(t)$ is the excitation injected to the system

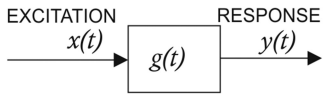

Fig. 3. Typical block diagram of the system impulse response measurement.

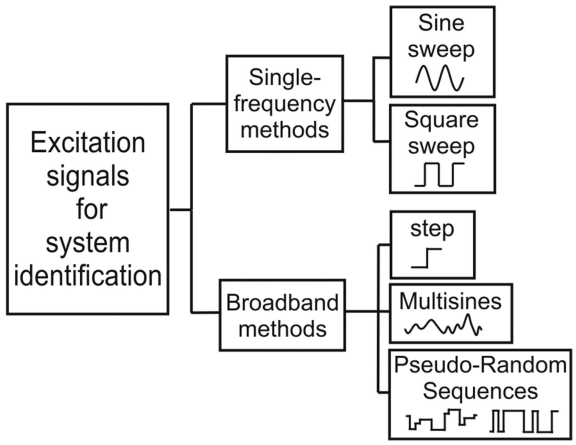

Fig. 4. Different excitation signals used for system identification.

input, which generates the corresponding output response $y(t)$. Together, the $x(t)$ and $y(t)$ defines the system impulse-response $g(t)$. For the system measurement, it is important that the excitation signal $x(t)$ is a predefined signal with known frequency response characteristics in order to generate any reliable response for the system output.

The different excitation signal types are illustrated in Fig. 4 in which the excitation signals can be roughly divided into two categories. These are the single-frequency signals and the broadband signals. Single-frequency signals have energy at one fundamental frequency while broadband signals have energy at multiple frequency harmonics. The single-frequency sweeps have higher measurement time than broadband signals due to the fact that the specified frequencies must be excited with separate signals at different fundamental frequency. However, the SNR is a lot higher because the energy of the signal is concentrated on the fundamental frequency [28].

For the battery impedance measurements, the excitation is typically injected as the current reference for a battery. The conventional method for battery impedance characterization is the EIS method in which a sine-sweep excitation is utilized [14]–[16]. The EIS provides accurate and reliable results and is widely used for offline applications. Due to the single-frequency characteristics, the EIS is not the most practical for online measurements and simplifications are required in order to reduce the complexity and measurement time [17]–[19]. The complexity of the signal can be reduced by using a square-sweep instead of sine-sweep [20] but the method is still very slow. The measurement time can be significantly reduced by the broadband methods shown in Fig. 4. From such methods, the step-based methods are the easiest to implement but the accuracy is drastically reduced, especially for the high-frequency response [21]–[24]. To achieve both the low measurement time and low complexity, multisines [24], [25] and PRS signals [28], can be utilized. Especially the PRS signals are attractive for online applications since the number of required signal levels can be reduced to the minimum of two levels (the PRBS), which significantly reduces the complexity of the signal implementation. Moreover, the accuracy is also relatively high. As a drawback, the operation of the PRBS is limited for identification of linear systems, which is a challenging aspect for battery impedance measurements due to the nonlinear behavior of batteries [20], [26]–[28]. However, PRS signals with three levels (ternary sequence) can be designed in a way that the nonlinearities at specific frequency harmonics can be reduced yielding to improved accuracy of the nonlinear system measurements [28]–[30], [32]. The generating algorithms of both PRS signals, the PRBS and the ternary sequence, are carefully studied and presented in the following sections.

A. PRBS Method

The PRBS signal used in this paper is the maximum-length binary sequence (MLBS). The MLBS theory is based on the linear recurrence relation algorithm [28] defined as

$$s(i) = \sum_{r=1}^{n} C_r s(i-r), \quad \text{mod } 2 \tag{2}$$

which yields to a binary sequence with possible values of 0 and 1. The variable C contains the coefficients of the arbitrary primitive polynomial of order n in modulo 2. It should be noted that any primitive polynomial coefficients can be used and the selection is up to the user. The n determines the length of the MLBS period as $N = 2^n - 1$. The first n elements in s must be initialized to any combination of 0 and 1 excluding the zero vector. The sequence is typically remapped to values -1 and 1 to give zero mean for the sequence. In order to avoid confusion, the term PRBS is used over the MLBS in the following parts of the paper [28].

B. Ternary-Sequence Method

The ternary sequence used in this paper is the quadratic-residue ternary (QRT) sequence [29], [30]. The QRT sequence can be obtained for any sequence length N for which $N/2$ is a prime. The sequence is formed by means of a quadratic residue algorithm. That is, $v(i), i = 1, 2...N$, is mapped to signal levels 1, -1, and 0 as follows:

$$v(i) = 1 \quad \text{if } i \text{ is square modulo } N/2$$
$$v(i) = -1 \quad \text{if } i \text{ is not square modulo } N/2$$
$$v(i) = 0 \quad \text{if } i = 0 \text{ modulo } N/2.$$

The sequence $v(i)$ is now formed by two consecutive subsequences from which the QRT sequence can be obtained by inverting the alternate elements in $v(i)$ as

$$s_{\text{QRT}}(i) = -1^{i-1} v(i) \quad i = 1, 2..N, \text{ modulo } N/2. \tag{3}$$

As a result, the generated QRT sequence s_{QRT} has three signal levels and zero power at all even-order harmonics. For the sake of simplicity, the QRT sequence is treated as a ternary sequence in the following parts of this paper.

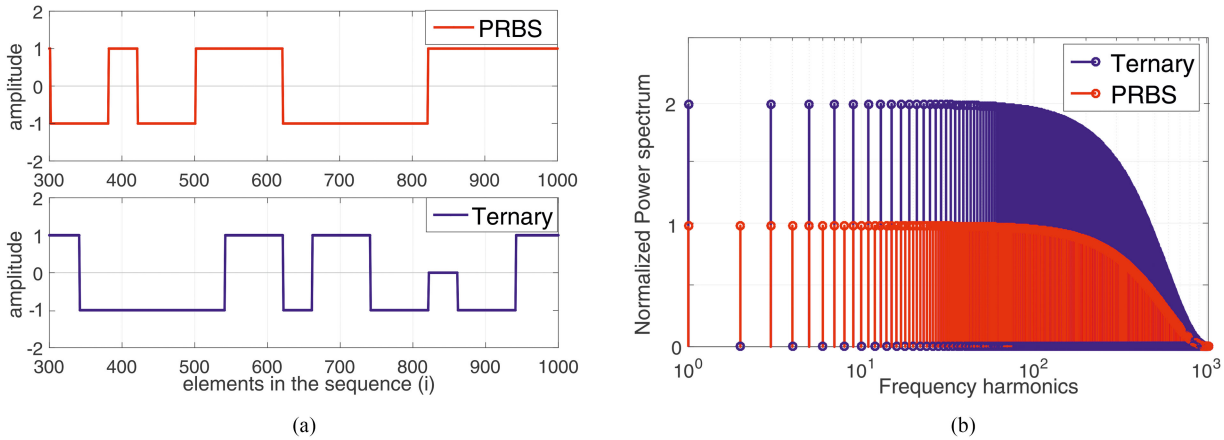

Fig. 5. (a) Time-domain characteristics of studied PRS signals. (b) Frequency-domain power spectrums of studied PRS signals.

C. Properties of the Presented Sequences

In time-domain, the difference between the PRBS and ternary sequence is that the ternary sequence is implemented with one extra signal level, as shown in Fig. 5(a). The differences in frequency domain are more characteristic as illustrated in Fig. 5(b), where normalized power spectrums of the sequences with similar amplitude and length are given. The ternary sequence has no power at even-order harmonics; thus, the nonlinear distortion at these harmonics will not affect to the nonzero harmonics and the measurements [29], [30]. The power at the first frequency harmonic in Fig. 5(c) is determined for the PRBS as

$$P_{\text{PRBS}}(1) = \frac{2A^2(N+1)}{N^2} \tag{4}$$

where A is the amplitude and N is the length of the sequence. The corresponding power for the ternary sequence is given as

$$P_{\text{Ternary}}(1) = \frac{4A^2}{N}. \tag{5}$$

From (4) and (5), it is observed that the power of the ternary sequence is approximately twice the power of the PRBS, which can also be seen from Fig. 5(b) [28], [29]. Thus, the SNR is also doubled according to

$$\text{SNR} = \frac{P_{\text{signal}}}{P_{\text{noise}}}. \tag{6}$$

It can be concluded from (4)–(6) that, for similar values of N, the amplitude of the ternary sequence can be reduced by a factor of $1/\sqrt{2}$ to obtain equal SNR than the PRBS. This gives more freedom for the amplitude design of the ternary sequence. Besides the amplitude, N also has significant effect on the signal power and SNR but is typically more significant design parameter to obtain desired measurement bandwidth and resolution. However, the number of possible N values is significantly higher for the ternary sequence than for the PRBS. This also gives more freedom for the ternary sequence to design the power and frequency content of the signal [36].

For both PRS signals, the frequency content is determined by the generation frequency f_{gen}, which is theoretically the maximum frequency that the sequence has energy at. Due to the decreasing power of the nonzero harmonics toward higher frequencies [see Fig. 5(b)], the usable bandwidth of the measurements is less than f_{gen} in reality. The guideline for appropriate bandwidth is given in [28] equaling to $\approx 0.45 * f_{\text{gen}}$. Together, N and f_{gen} determines the frequency resolution of the sequences as

$$f_{\text{res}} = \frac{f_{\text{gen}}}{N} \tag{7}$$

which is also the lowest frequency at which the signal has energy. For the battery impedance measurements, f_{res} is important parameter because it determines also the minimum time consumed for the whole measurement as $t_{\text{meas}} = 1/f_{\text{res}}$. This becomes especially important when measuring the diffusion region of the impedance realized at very low frequencies, which correspond to long response time.

IV. Experiments

The measurements were carried out with the ternary sequence and the PRBS injections for a $LiFePO_4$ battery cell with a nominal voltage of 3.3 V and a capacity of 2.5 Ah at three different temperatures, which were 24, 34, and 41 °C. The setup configuration is shown in Fig. 6(a) where the bidirectional power supply is used to inject the excitations as the current reference. The excitations are configured to have zero offset to keep the SOC at a steady state during the measurements, thus, minimizing the nonlinearities of the measured impedance. The changing current direction within the excitation pulse is considered not to affect the measurements since the dynamics of the impedance are similar during charging and discharging [23]. The voltage and current measurements, i_{meas} and v_{meas}, are recorded as vectors whose lengths are equal to the excitation length given as the current reference i_{ref}. In the frequency-response-analysis block, the voltage and current measurements are applied by discrete Fourier transform to obtain the impedance frequency spectrum. The filtering of the results is implemented with a MAF. Both PRS signals were generated by a software available in [30].

The laboratory setup and the used equipment are shown in Fig. 6(b). The excitations were injected by the data-acquisition (DAQ) device as the current reference to a bidirectional power supply. The data are also recorded from the measurement probes

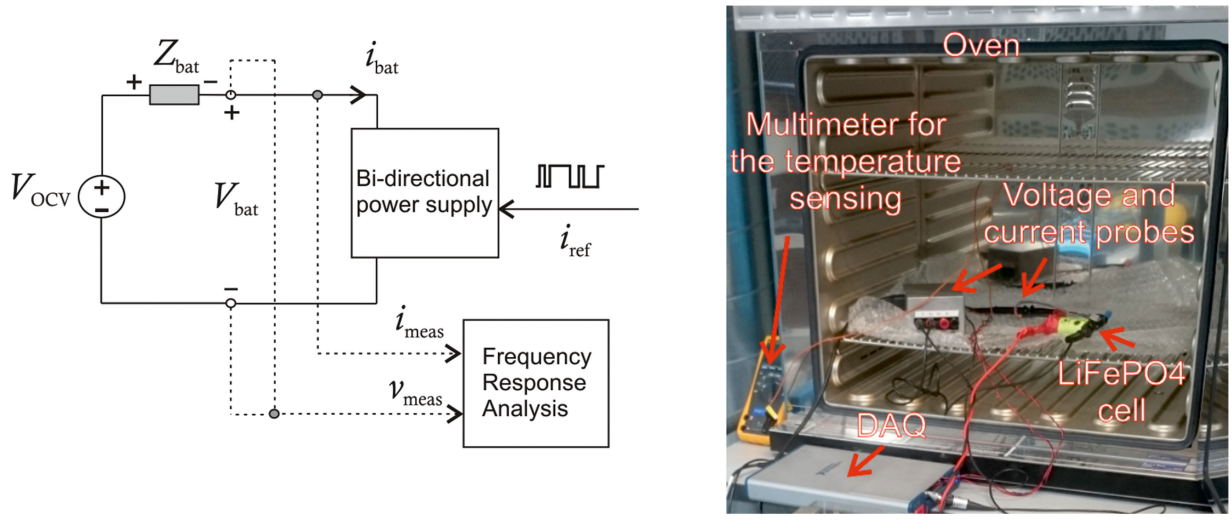

(a) (b)

Fig. 6. (a) Measurement setup configuration for the experiments. (b) Laboratory setup.

TABLE I
INJECTION PARAMETERS FOR SENSITIVITY ANALYSIS

	f_{gen}	N	frequency band	f_s
Ternary-sequence	7 kHz	32762	$210\,mHz - 3.15\,kHz$	35 kHz
MLBS	7 kHz	32767	$210\,mHz - 3.15\,kHz$	35 kHz

by the DAQ, which is connected to the computer where data are postprocessed. The measurements were carried out by applying the measurement sweep over the whole SOC and considering a SOC resolution of 10%. The desired SOC level was reached by discharging the battery with a current of 1 C. The SOC was monitored by the coulomb-counting method [26]. Before each measurement sweep, the battery is left on hold for 30 min to allow the battery voltage to reach its thermo-dynamic stability. The EIS reference measurement were carried out with a separate EIS analyzer setup.

Before validating the PRBS and the ternary-sequence measurements to the EIS reference, the amplitude sensitivity analysis and filtering design are carried out for both PRS signals in the following sections. The design parameters of both PRS injections for the amplitude design are listed in Table I, where the f_s denotes the sampling frequency. The generation frequency and sequence lengths were selected to cover a bandwidth that captures the end of the diffusion part, as well as, the beginning of the ohmic region of the used $LiFePO_4$ cell.

A. Sensitivity Analysis

The effect of the amplitude sensitivity to the impedance measurements is investigated by the standard deviation (STD) of the impedance magnitude over the used frequency spectrum. The STD is mathematically defined as

$$\sigma = \sqrt{\frac{1}{N}\sum_{i=1}^{N}(Z_i - Z_{mean})^2} \tag{8}$$

where Z_i is the ith sample of the measured impedance, Z_{mean} is the average over the whole measured impedance, and N is the length of the measured impedance vector. The STD can be regarded as an rms-value of the measurement deviation around the Z_{mean}. Therefore, it is an equally informative indicator than the SNR for measuring the accuracy of the measurements. However, the STD provides the information about the noise in the measurements, which is why it is used for the amplitude sensitivity analysis instead of the SNR given in (6).

The STD is analyzed at different excitation current amplitudes as C-rates, which corresponds the current normalized by the capacity of the battery. The current of 1 C was determined to be the upper limit for the amplitude design due to the protection limits of the power supply that are violated with higher currents. The measured impedance STD as a function of C-rate is illustrated at varying temperatures and SOC values in Fig. 7(a) and (b), respectively. The temperature affects to the STD by increasing it as the temperature increases while the SOC does not have noticeable impact on the STD. Moreover, the STD of the ternary sequence is lower than that of the PRBS.

Due to the observations made above, the amplitude design of the injections is based on the STD at worst case temperature, which is at 41 °C. To have a better understanding of the STD, the STD is normalized by the mean value of the measured impedance magnitude illustrated in Fig. 7(c). For the currents greater than 0.4 C, the normalized STD is not significantly reduced and the selection guideline was selected to choose the current at which the normalized STD is 5% for both PRS signals. According to Fig. 7(c), the 5% point equals 0.55 C = 1.375 A for the ternary sequence and 0.8 C = 2 A for the PRBS. The ratio of the amplitudes is very close to $1/\sqrt{2} \approx 0.707$ for each STD values, which results from the increased SNR of the ternary sequence as discussed in Section III-C.

B. Filtering of the Measurement Results

The simple MAF is used for filtering the measurement data due to its simplicity and relatively good performance [34]. Instead of time-domain filtering, the MAF is applied to frequency-domain data in order to ensure the uniqueness of the PRS signals. This significantly changes the design guidelines and

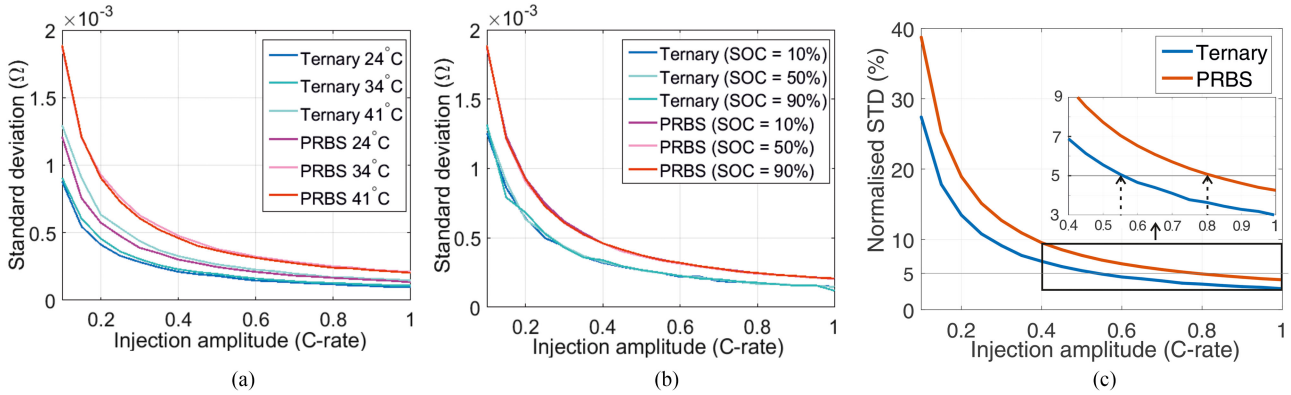

Fig. 7. (a) STD of the impedance measurements as a function of injection amplitude at different temperatures at 50% of SOC. (b) STD of the impedance measurements as a function of injection amplitude at different SOC values at 41 °C. (c) Normalized STD of the ternary sequence and PRBS as a function of injection amplitude at 50% of SOC and at 41 °C.

performance of the MAF compared to time-domain filtering. The simple MAF is defined as

$$x_{\mathrm{MAF}}(i) = \frac{1}{M}\sum_{k=-d}^{d} x(i+k) \tag{9}$$

where M is the window length, i is the element index in the dataset, and

$$d = \frac{M-1}{2} \tag{10}$$

which represents the delay of the MAF. The MAF enhances the SNR of the measurements by a factor $\sqrt{M}$ since the noise in the measurements is expected to have white-noise Gaussian distribution [36]. However, the MAF in (9) cannot be applied to the first d elements in the data. Therefore, the estimates for the first d data points are obtained by increasing the window starting from $M = 1$ until the desired M is reached. The algorithm is mathematically expressed as

$$x_{\mathrm{MAF}}(i) = \frac{1}{2i-1}\sum_{k=-(i-1)}^{i-1} x(i+k), i = 1...d \tag{11}$$

which is changed to (9) for $i > d$. The effect of the MAF delay for the impedance plot is illustrated in Fig. 8, where several different window sizes are applied to ternary-sequence battery impedance measurements at 41 °C. Each window will follow the black curve, i.e., (11), until the index corresponding to d is reached. Therefore, if there are changing trends in the data during the effect of d, the curve will be dislocated. This is especially the case for the end of the diffusion part, which is lifted from the average of the unfiltered data for higher windows than 21. The same occurs also for the top of the semicircle for very high windows. Thus, the selection of the optimal window length is highly depending on the data indices at the end of the diffusion region and the top of the semicircle. The data indices at these points are illustrated in Fig. 9, where unfiltered impedance data at different temperatures are shown as bode plot. The yellow curve in Fig. 9 corresponds the impedance in Fig. 8 and shows that the end of the diffusion region is taking place at 25th data index while the top of the semicircle is obtained at a 200th data index. Fig. 8 shows that the window lengths greater than the foregoing indices

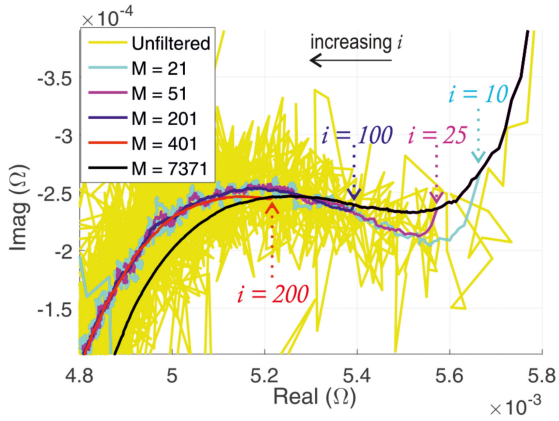

Fig. 8. Impedance Nyquist plots obtained with ternary sequence at 41 °C and at 50% of SOC with different MAF window lengths. The colored indices i represents the data index where the corresponding MAF starts to adapt to the data.

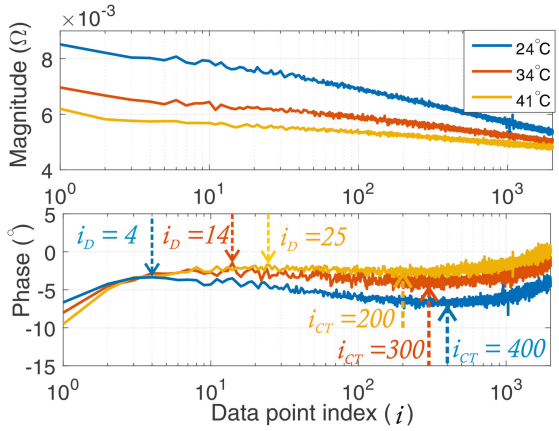

Fig. 9. Bode plot representation of the unfiltered impedance data obtained with the ternary sequence at 50% of SOC. Colored markings i_{D} represents the end of the diffusion part indices and i_{CT} the top of the semicircle indices of the impedance at the corresponding temperature.

are dislocating the corresponding part of the impedance plot. Thus, in order to prevent the data from dislocating, the window size should not exceed the data index at which the corresponding region bound is reached. However, it can be seen from Fig. 9

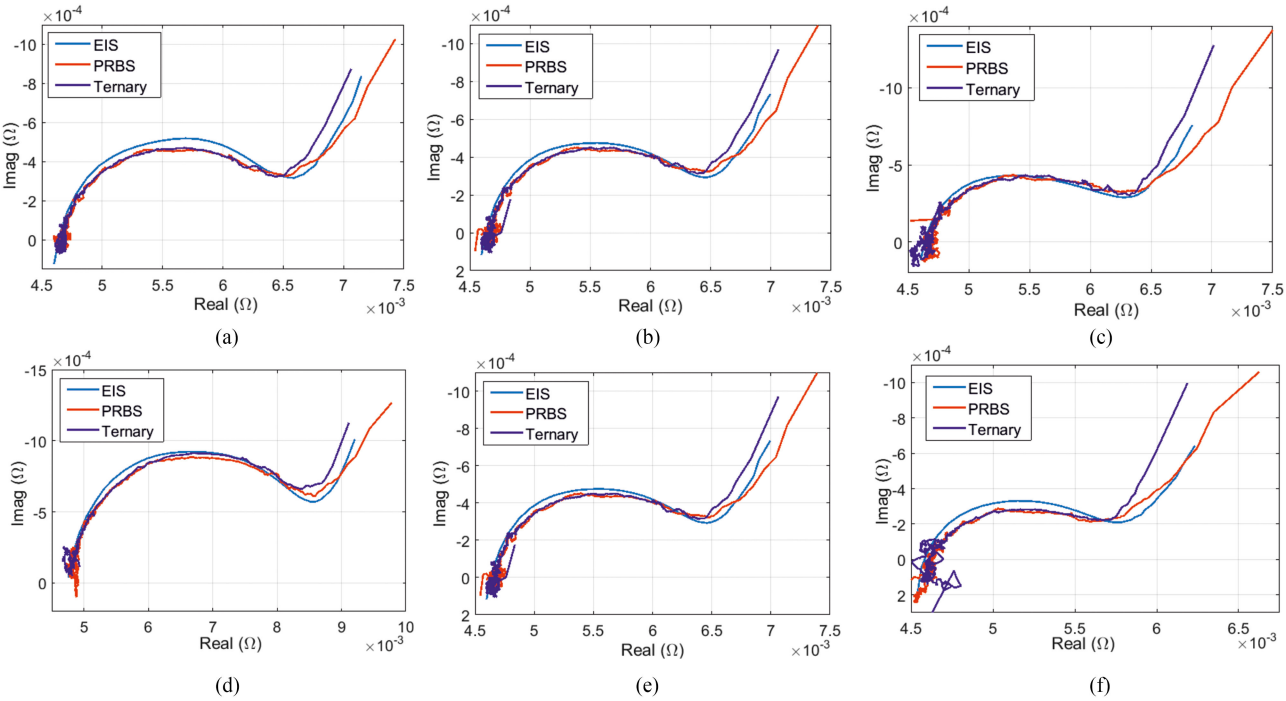

Fig. 10. Impedance Nyquist plot at 34 °C and (a) at 20% of SOC, (b) 50% at of SOC, and (c) at 80% of SOC. Impedance Nyquist plot at 50% of SOC and (d) at 24 °C, (e) at 34 °C, and (f) at 41 °C.

TABLE II
INJECTION PARAMETERS FOR MEASUREMENTS AND PERFORMANCE VALIDATION

	EIS	Ternary	PRBS
Amplitude	0.7A-2 A	1.375 A	2 A
First measured freq.	206 mHz	220 mHz	220 mHz
Last measured freq.	3.7 kHz	3.15 kHz	3.15 kHz
f_{gen}	-	7 kHz	7 kHz
f_s	-	35 kHz	35 kHz
N	-	32767	32762
MAF window	-	25 and 120	50 and 240
Measurement time	1 min	4.7 s	4.7 s

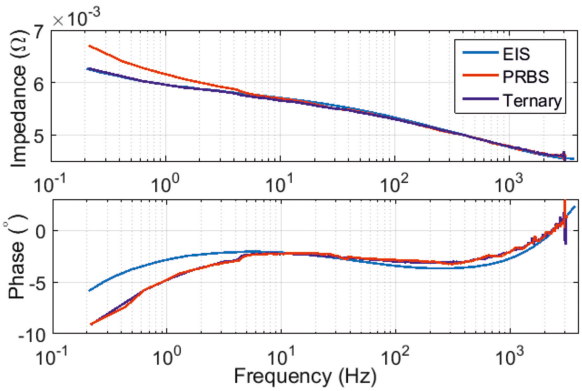

Fig. 11. Impedance Bode plot measured with different excitations at 41 °C and 50% of SOC.

that the indices of the impedance region bounds will change as a function of the temperature and the window length can be difficult to be selected adaptively.

Based on the abovementioned discussion, the MAF of two fixed-length overlapping windows are used for the filtering. The window sizes are selected according to the smallest indices at the end of the diffusion part and at the top of the semicircle in Fig. 9 at 41 °C. This yields to first window equaling to 25 for the ternary sequence. This will slightly affect to the smoothing of the measurements at 24 and 34 °C by dislocating the end of the diffusion region. The latter window is selected to be sufficiently smaller than the indice at the top of the semicircle to ensure the good performance of the MAF. Therefore, the window size of 120 is selected for the latter window for the ternary sequence. The windows for the PRBS can be twice as long due to the twice as dense frequency resolution. Therefore, the window lengths of 50 and 240 are used for the PRBS. An overlap of 25% is considered for the windows to minimize the transient effect when the windows are changed. With the designed configurations, the SNR can be maximized while minimizing the dislocation of the measurements results.

V. RESULTS AND VALIDATION

The design parameters for the measurements and validation are listed in Table II. The accuracy of the results in Fig. 10 is validated by the RMSE given as

$$\epsilon_{\text{err}} = \sqrt{\frac{1}{N}\sum_{i=1}^{N}\left(1-\frac{Z_{\text{meas}}(i)}{Z_{\text{ref}}(i)}\right)^2} \tag{12}$$

where Z_{meas} is the measurements of the PRBS and the ternary sequence, and Z_{ref} is the EIS reference data. Due to the logarithmic frequency distribution, the EIS impedance results are realized with only 35 data points, which is much less than the impedance

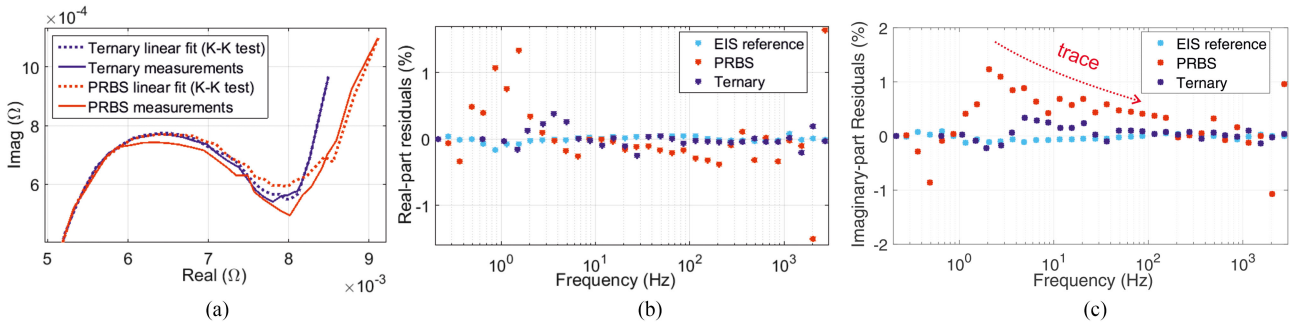

Fig. 12. (a) Fitted impedances from the Kronig–Kramers test compared to the measured impedances at 25 °C and 50% of SOC. (b) Real-part residuals from the Kronig–Kramers compliance test applied to impedance measurements at 25 °C and 50% of SOC. (c) Imaginary-part residuals from the Kronig–Kramers compliance test applied to impedance measurements at 25 °C and 50% of SOC.

TABLE III
RMS ERRORS OF THE PRS MEASUREMENTS WITH RESPECT TO THE EIS RESULTS AT VARIOUS SOCS AND TEMPERATURES

PRBS			
	SOC 30%	SOC 50%	SOC 80%
24°C	8.3%	7.3%	7.4%
34°C	6.8%	5.1%	4.3%
41°C	6.3%	4.0%	3.2%
Ternary			
	SOC 30%	SOC 50%	SOC 80%
24°C	2.9%	2.1%	2.3%
34°C	2.1%	1.1%	0.5%
41°C	1.6%	0.7%	1.1%

measurements with the designed PRS signals whose harmonics are linearly distributed. Therefore, the frequency harmonics in the PRBS and the ternary-sequence impedance results that are closest to each corresponding harmonics in the EIS data are chosen to be applied in (9).

The validity of the applied PRS measurements is also analyzed by applying linear Kronig–Kramers compliance test to the measurements [35]. In the test, the impedance data are fitted to a linearized impedance model from which the residuals of the real- and imaginary parts are observed. According to the test, the data can be regarded corrupted if the residuals are following a clear trace whereas uncorrupted data are realized with white noise distribution of the residuals. The test is a useful tool for validating how well the impedance can be linearly fitted, which also indicates the usability of the results for battery state estimation [24]. The method is applied by using a software introduced in [24].

The results from the PRS measurements referenced to the EIS measurements are illustrated in Fig. 10 at different SOCs and temperatures. It can be observed that the PRS results are matching relatively well to the EIS reference data at all temperatures and SOC values. The biggest differences are observed at the diffusion region where all excitations are differing from each other, which makes the comparison of the PRS signals challenging. However, the magnitude spectrum in Fig. 11 reveals the improved accuracy of the ternary sequence at the diffusion region, where it shows better match to the EIS than the PRBS. The performance is also validated by the measurement errors in Table III, which are comprehensively smaller for the ternary sequence than for the PRBS. Moreover, the results of the linear Kronig–Kramers compliance test shown in Fig. 12 reveals the better compliance of the ternary-sequence results. The test was applied to the measurements at 25 °C, which listed the greatest error in Table III. The residuals from the test in Fig. 12(b)–(c) are having a white-noise distribution for the ternary sequence, which validates the validity of the measurements. For the PRBS, a clear trace can be observed particularly from the imaginary part residuals, as illustrated in Fig. 12(c), which indicates that the measurement data is corrupted at low and medium frequencies. This can also be seen from the impedance plots in Fig. 12(a), where systematic error is observed on most parts of the impedance curve for the PRBS fit while the ternary-sequence fit is matching the measurements accurately. Moreover, the magnitude of the residuals are comprehensively smaller for the ternary sequence than for the PRBS.

It can be observed that the errors in Table III are generally slightly increasing as the temperature is decreased. This may indicate that the performance of both PRS signals may be insufficient at very low temperatures at which the performance of the PRS signals should also be validated. However, the measurements were not possible to be performed at lower temperatures due to the lack of appropriate laboratory devices. Nevertheless, the errors are still very small and the error increase can be explained by the differences in the measurement setups since the EIS was performed with a commercial EIS analyzer. For more reliable comparison, the EIS should have been applied with the same setup that the PRS signals but this was not possible due to the limitation of the bidirectional power supply used for PRS measurements. Moreover, the slightly increased error can also be explained by the MAF window length that, for the sake of more relevant comparison between the PRS, was optimized for the measurements at 41 °C.

The significant benefit of PRS signals over the EIS is the reduced measurement time, which was over 12 times faster for both PRS signals. Moreover, the complexity of the PRS signals is very low since only two and three signal levels are required. From the applied PRS signals, the ternary sequence showed better performance at the low-frequency region even with lower excitation amplitude. With the increased bandwidth and accuracy of the measurements, the ternary sequence holds the potential to be scaled for other Li-ion chemistries. Thus, the ternary sequence is attractive alternative for the conventional

EIS for utilizing the impedance measurements in online battery applications.

VI. Conclusion

This paper demonstrated the use of two PRS excitation signals, the PRBS and the ternary sequence, for fast battery impedance measurements. Both sequences were comprehensively designed and validated to reliable EIS reference measurements in various operating conditions for a $LiFePO_4$ battery cell. The measurement time with both PRS signals was only 4.7 s, which is 12 times less than that of the EIS for which the measurement time was 1 min. The complexity of the PRS signals is also significantly lower than for the EIS, and the PRS signals could be implemented to an application with low-cost microprocessors. The practical measurements showed that the performance of the ternary sequence is higher, especially at the low frequencies where the PRBS results were slightly distorted. Another advantage of the ternary sequence is that the signal allows using smaller injection amplitude compared to the PRBS. Moreover, the linear Kronig–Kramers compliance test validated the performance of the ternary sequence. By contrast, the PRBS measurements were found to be corrupted mostly due to the nonlinear distortion affected to the measurements, especially at the diffusion region of the battery impedance. By considering the aforementioned aspects, the ternary sequence is a very attractive alternative for battery impedance measurement and practical for online battery applications in electric vehicles and in stationary energy storages with scalability to other Li-ion chemistries.

References

[1] S. Vazquez, S. M. Lukic, E. Galvan, L. G. Franquelo, and J. M. Carrasco, "Energy storage systems for transport and grid applications," *IEEE Trans. Ind. Electron.*, vol. 57, no. 12, pp. 3881–3895, Dec. 2010.

[2] G. Berckmans, M. Messagie, J. Smekens, N. Omar, L. Vanhaverbeke, and J. V. Mierlo, "Cost projection of state of the art lithium-ion batteries for electric vehicles up to 2030," *Energies*, vol. 10, no. 9, Sep. 2017, Art. no. 1314.

[3] H. Rahimi-Eichi, U. Ojha, F. Baronti, and M. Chow, "Battery management system: An overview of its application in the smart grid and electric vehicles," *IEEE Ind. Electron. Mag.*, vol. 7, no. 2, pp. 4–16, Jun. 2013.

[4] J. Rivera-Barrera, N. Muñoz-Galeano, and H. Sarmiento-Maldonado, "SoC estimation for lithium-ion batteries: Review and future challenges," *Electronics*, vol. 6, no. 4, Nov. 2017, Art. no. 102.

[5] M. Berecibar, I. Gandiaga, I. Villarreal, N. Omar, J. Van Mierlo, and P. Van den Bossche, "Critical review of state of health estimation methods of Li-ion batteries for real applications," *Renewable Sustain. Energy Rev.*, vol. 56, pp. 572–587, Apr. 2016.

[6] D. I. Stroe, M. Swierczynski, A. I. Stan, V. Knap, R. Teodorescu, and S. J. Andreasen, "Diagnosis of lithium-ion batteries state-of-health based on electrochemical impedance spectroscopy technique," in *Proc. IEEE Energy Convers. Congr. Expo.*, Sep. 2014, pp. 4576–4582.

[7] D. I. Stroe, M. Swierczynski, S. K. Kær, and R. Teodorescu, "Degradation behavior of lithium-ion batteries during calendar ageing—The case of the internal resistance increase," *IEEE Trans. Ind. Appl.*, vol. 54, no. 1, pp. 517–525, Jan./Feb. 2018.

[8] J. Vetter, P. Nov, M. R. Wagner, and C. Veit, "Ageing mechanisms in lithium-ion batteries," *J. Power Sources*, vol. 147, pp. 269–281, 2005.

[9] D. V. Do, C. Forgez, K. El, K. Benkara, G. Friedrich, and S. Member, "Impedance observer for a Li-ion battery using kalman filter," *IEEE Trans. Veh. Technol*, vol. 58, no. 8, pp. 3930–3937, Oct. 2009.

[10] U. Westerhoff, T. Kroker, K. Kurbach, and M. Kurrat, "Electrochemical impedance spectroscopy based estimation of the state of charge of lithium-ion batteries," *J. Energy Storage*, vol. 8, pp. 244–256, 2016.

[11] J. Xu, C. C. Mi, B. Cao, and J. Cao, "A new method to estimate the state of charge of lithium-ion batteries based on the battery impedance model," *J. Power Sources*, vol. 233, pp. 277–284, 2013.

[12] A. Zenati, P. Desprez, and H. Razik, "Estimation of the SOC and the SOH of Li-ion batteries, by combining impedance measurements with the fuzzy logic inference," in *Proc. 36th Annu. Conf. IEEE Ind. Electron. Soc.*, Nov. 2010, pp. 1773–1778.

[13] H. Dai, B. Jiang, and X. Wei, "Impedance characterization and modeling of lithium-ion batteries considering the internal temperature gradient," *Energies*, vol. 11, no. 1, Jan. 2018, Art. no. 220.

[14] S. Skoog and S. David, "Parameterization of linear equivalent circuit models over wide temperature and SOC spans for automotive lithium-ion cells using electrochemical impedance spectroscopy," *J. Energy Storage*, vol. 14, pp. 39–48, 2017.

[15] E. Unamuno, L. Gorrotxategi, I. Aizpuru, U. Iraola, I. Fernandez, and I. Gil, "Li-ion battery modeling optimization based on electrical impedance spectroscopy measurements," in *Proc. Int. Symp. Power Electron., Elect. Drives, Autom. Motion*, 2014, pp. 154–160.

[16] E. Karden, S. Buller, and R. W. De Doncker, "A method for measurement and interpretation of impedance spectra for industrial batteries," *J. Power Sources*, vol. 85, no. 1, pp. 72–78, 2000.

[17] W. Huang and J. A. Qahouq, "An online battery impedance measurement method using DC-DC power converter control," *IEEE Trans. Ind. Electron.*, vol. 61, no. 11, pp. 5987–5995, Nov. 2014.

[18] X. Wei, X. Wang, and H. Dai, "Practical on-board measurement of lithium-ion battery impedance based on distributed voltage and current sampling," *Energies*, vol. 11, no. 1, Jan. 2018, Art. no. 64.

[19] E. Din, C. Schaef, K. Moffat, and J. T. Stauth, "A scalable active battery management system with embedded real-time electrochemical impedance spectroscopy," *IEEE Trans. Power Electron.*, vol. 32, no. 7, pp. 5688–5698, Jul. 2017.

[20] R. Al Nazer, V. Cattin, P. Granjon, M. Montaru, and M. Ranieri, "Broadband identification of battery electrical impedance for HEVs," *IEEE Trans. Veh. Technol*, vol. 62, no. 7, pp. 2896–2905, Sep. 2013.

[21] J. A. Abu Qahouq and Z. Xia, "Single-perturbation-cycle online battery impedance spectrum measurement method with closed-loop control of power converter," *IEEE Trans. Ind. Electron*, vol. 64, no. 9, pp. 7019–7029, Sep. 2017.

[22] Z. Xia and J. A. Qahouq, "Method for online battery AC impedance spectrum measurement using DC-DC power converter duty-cycle control," in *Proc. Conf. Proc. IEEE Appl. Power Electron. Conf. Expo.*, 2017, no. 1, pp. 1999–2003.

[23] D.-I. Stroe, M. Swierczynski, A.-I. Stroe, and S. Knudsen Kær, "Generalized characterization methodology for performance modelling of lithium-ion batteries," *Batteries*, vol. 2, no. 4, Dec. 2016, Art. no. 37.

[24] A. Lasia, *Electrochemical Impedance Spectroscopy and Its Applications*. New York, NY, USA: Springer, 2014.

[25] D. A. Howey, P. D. Mitcheson, S. Member, V. Yufit, G. J. Offer, and N. P. Brandon, "Motor controller excitation," *IEEE Trans. Veh. Technol*, vol. 63, no. 6, pp. 2557–2566, Jul. 2014.

[26] J. Sihvo, T. Messo, T. Roinila, and R. Luhtala, "Online internal impedance measurements of Li-ion battery using PRBS broadband excitation and Fourier techniques: Methods and injection design," in *Proc. Int. Power Electron. Conf.*, May 2018, pp. 2470–2475.

[27] A. J. Fairweather, M. P. Foster, and D. A. Stone, "Battery parameter identification with pseudo random binary sequence excitation (PRBS)," *J. Power Sources*, vol. 196, no. 22, pp. 9398–9406, 2011.

[28] K. Godfrey, *Perturbation Signals for System Identification*. Englewood Cliffs, NJ, USA: Prentice-Hall, 1993.

[29] K. Godfrey, H. Barker, and A. Tucker, "Comparison of perturbation signals for linear system identification in the frequency domain," *IEE Proc.-Control Theory Appl.*, vol. 146, no. 6, pp. 535–548, 1999.

[30] A. H. Tan and K. R. Godfrey, "The generation of binary and near-binary pseudorandom signals: An overview," *IEEE Trans. Instrum. Meas.*, vol. 51, no. 4, pp. 583–588, Aug. 2002. [Online]. Available: http://www.eng.warwick.ac.uk/EED/DSM/prs.htm

[31] T. Roinila and T. Messo, "Online grid-impedance measurement using ternary-sequence injection," *IEEE Trans. Ind. Appl.*, vol. 54, no. 5, pp. 5097–5103, Sep. 2018.

[32] J. Sihvo, T. Messo, T. Roinila, and D. I. Stroe, "Online identification of internal impedance of Li-ion battery cell using ternary-sequence injection," in *Proc. IEEE Energy Convers. Congr. Expo.*, 2018, pp. 1–7.

[33] J. J. Giner-Sanz, E. M. Ortega, and V. Pérez-Herranz, "Optimization of the perturbation amplitude for EIS measurements using a total harmonic distortion based method," *J. Electrochemical Soc.*, vol. 165, no. 10, pp. E488–E497, Jul. 2018.

[34] S. Golestan, M. Ramezani, J. M. Guerrero, F. D. Freijedo, and M. Monfared, "Moving average filter based phase-locked loops: Performance analysis and design guidelines," *IEEE Trans. Power Electron.*, vol. 29, no. 6, pp. 2750–2763, Jun. 2014.
[35] B. A. Boukamp, "A linear Kronig-Kramers transform test for immittance data validation," *J. Electrochemical Soc.*, vol. 142, no. 6, pp. 1885–1894, Jun. 1995.
[36] N. Storey, *Electronics: A System Approach*, 4th ed. London, U.K.: Pearson, 2009.

Jussi Sihvo (S'18) received the M.Sc. degree in electrical engineering from the Tampere University of Technology, Tampere, Finland, in 2018. Since then, he has been a doctoral student with the Faculty of Information Technology and Communication Sciences, Tampere University, Tampere.

His research interests include modeling, diagnostics, and analysis of energy-storage systems and grid-connected converters.

Daniel-Ioan Stroe (M'11) received the Dipl.-Ing. degree in automatics from the Transilvania University of Braşov, Braşov, Romania, in 2008, and the M.Sc. degree in wind power systems from Aalborg University, Aalborg, Denmark, in 2010. He has been with Aalborg University since 2010, from where he received the Ph.D. degree in lifetime modeling of lithium-ion batteries in 2014.

He is an Associate Professor with the Department of Energy Technology, Aalborg University, where he leads the Battery Storage Systems Research Programme and the Battery Systems Testing Lab. He was a Visiting Researcher with RWTH Aachen, in 2013. He has coauthored more than 100 journal and conference papers in various battery-related topics. His current research interests are in the area of energy storage systems for grid and e-mobility, lithium-based batteries testing, modeling, and diagnostics and their lifetime estimation.

Tuomas Messo (M'14) received the Ph.D. degree in electrical engineering from the Tampere University of Technology, Tampere, Finland, in 2014.

He is currently with GE Grid Solutions and holds the position of an Adjunct Professor with the Tampere University, Tampere, in the field of power electronics, where he also was an Assistant Professor between 2016 and 2019. His research interests include grid-connected three-phase power converters for renewable energy applications and microgrids, dynamic modeling, control design, impedance-based interactions in three-phase systems, and impedance design of grid-connected inverters.

Tomi Roinila (M'10) received the M.Sc. and Dr.Tech. degrees in automation and control engineering from the Tampere University of Technology, Tampere, Finland, in 2006 and 2010, respectively.

Since then, he has been as an Academic Research Fellow and an Academic Researcher with the Faculty of Engineering and Natural Sciences, Tampere University. His main research interests include modeling and control of grid-connected power-electronics system, analysis of power-electronics multiconverter systems, and analysis of energy-storage systems.